

# Nonlinear transport theory at the order of quantum metric

Zhen-Hao Gong<sup>†, 1</sup>, Z. Z. Du<sup>†, 2, 3</sup>, Hai-Peng Sun<sup>4</sup>, Hai-Zhou Lu<sup>1, 5, \*</sup> and X. C. Xie<sup>6, 7, 8</sup>

<sup>1</sup>*Department of Physics, State key laboratory of quantum functional materials, and Guangdong Basic Research Center of Excellence for Quantum Science, Southern University of Science and Technology (SUSTech), Shenzhen 518055, China*

<sup>2</sup>*International Quantum Academy, Shenzhen 518048, China*

<sup>3</sup>*Shenzhen Key Laboratory of Quantum Science and Engineering, Shenzhen 518055, China*

<sup>4</sup>*Institute for Theoretical Physics and Astrophysics, University of Würzburg, 97074 Würzburg, Germany*

<sup>5</sup>*Quantum Science Center of Guangdong-Hong Kong-Macao Greater Bay Area (Guangdong), Shenzhen 518045, China*

<sup>6</sup>*Interdisciplinary Center for Theoretical Physics and Information Sciences (ICTPIS), Fudan University, Shanghai 200433, China*

<sup>7</sup>*International Center for Quantum Materials, School of Physics, Peking University, Beijing 100871, China*

<sup>8</sup>*Hefei National Laboratory, Hefei 230088, China*

(Dated: March 25, 2025)

Quantum metric, a probe to spacetime of the Hilbert space, has been found measurable in the nonlinear electronic transport thus has attracted tremendous interest. However, without comparing with mechanisms tied to disorder, it is still unclear whether the quantum metric dominates in recent experiments. We exhaust all possible mechanisms of nonlinear transport under the same symmetry that the quantum metric emerges, by finding five more disorder-related mechanisms and their nonlinear conductivity formulas. With the help of the formulas, we derive the scaling law to identify distinct mechanisms in the recent experiments [Gao, et al., *Science* 381, 181 (2023); Wang, et al., *Nature* 621, 487 (2023)], determine nonzero nonlinear conductivity elements for all 122 magnetic point groups to guide future experiments, and calculate the nonlinear conductivity to explain the sophisticated features in the experiments of the even-layered  $\text{MnBi}_2\text{Ti}_4$  thin films. Our theory will facilitate future experiments and applications of nonlinear transport.

The nonlinear Hall effect is characterized by a transverse voltage nonlinearly dependent on the longitudinal driving current [Fig. 1(a)]. It has received tremendous attention because of its potentials as a measurement method [1–36], in device applications such as wireless rectification [37–39], and even inspiring new insights for the research of nonlinear optics [40–50]. More excitingly, the nonlinear Hall effect can be contributed by the quantum metric [51–56], the real part of quantum geometry [57–67], which measures the distance between quantum states, thus can provide spacetime insights to the challenges in condensed matter [68]. However, the disorder contributions, such as the side jump that shifts coordinates of electrons sideward and skew scattering that asymmetrically deflects electrons [Fig. 1(b)] [69], cannot be ignored [6], inspiring an increasing interest in searching for all possible mechanisms of the nonlinear transport [45, 70]. More importantly, without comparing with all possible mechanisms, e.g., higher-order terms tied to disorder, it is still unclear whether the quantum metric leads to the nonlinear Hall effect in the recent experiments [54, 55].

In this Letter, we aim to exhaust all the contributions to the nonlinear conductivities under the same symmetry that the quantum metric emerges, by treating the geometry and disorder on an equal footing. We find 5 new mechanisms at the order of quantum metric [Fig. 1(c)] and their explicit formulas. The formulas allow us to derive a scaling law that relates the nonlinear Hall con-

ductivity and linear longitudinal conductivity, to distinguish mechanisms in the recent experiments as from the quantum metric dipole [54] and from the 2nd-order skew scattering discovered here [55], respectively. The results are also verified by symmetry analysis and model calculation. The formulas also allow us to determine nonzero nonlinear conductivity elements for materials categorized by the magnetic point groups, as well as to calculate the nonlinear conductivity with realistic Hamiltonians, such as for even-layered  $\text{MnBi}_2\text{Te}_4$  thin films, to describe the sophisticated features in the experimental data [54, 55]. This theory is not only at the order of quantum metric but also a comprehensive description of the quadratic nonlinear transport.

*Mechanisms of Nonlinear Hall effect at the order of quantum metric.*— A Hall effect occurs when electrons driven by an electric field are deflected to the transverse direction. In the absence of magnetic field, three mechanisms may lead to the Hall effect linear in electric field  $\vec{E}$ , the Berry curvature, side jump, and skew scattering [69], as shown in Fig. 1(b). The Berry curvature [71] describes the curving of the Hilbert space of the Bloch states prevents electrons from going straight in a perfect crystal. In the presence of disorder, that is, imperfection of the crystal, the side jump shifts sideward the coordinates of spin-up and spin-down electrons oppositely, and skew scattering symmetrically deflects spin-up and spin-down electrons due to the spin-orbit coupling. The three mechanisms are  $\propto \vec{E}$ , so the 2nd-order mixing of them

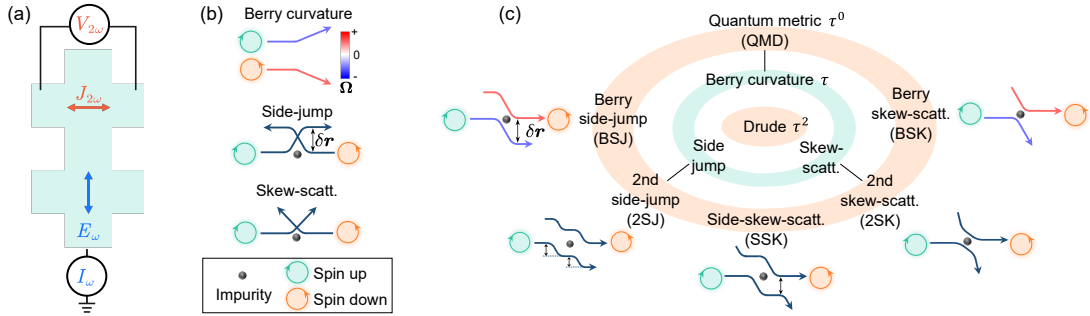


FIG. 1. (a) Nonlinear Hall effect is measured experimentally as a double-frequency transverse voltage  $V_{2\omega}$  driven by a low-frequency current  $I_\omega$  (10-1000 Hz), or calculated theoretically as a current density  $J_{2\omega}$  driven by an electric field  $E_\omega$ . (b) Three mechanisms for the anomalous Hall effect [69], Berry curvature  $\Omega$ , side jump (which shifts sideward the coordinates of spin-up and spin-down electrons oppositely by  $\delta r$ ), and skew scattering (which asymmetrically deflects spin-up and spin-down electrons), could serve as the building blocks for the mechanisms of the nonlinear Hall effect. (c) Hierarchy of the nonlinear transport, including (i) the Drude mechanism in the absence of time-reversal ( $\mathcal{T}$ ) and inversion ( $\mathcal{P}$ ) symmetries; (ii) the Berry curvature dipole [1, 2], side jump, and skew scattering mechanisms [6, 10] under  $\mathcal{T}$  but without  $\mathcal{P}$  symmetry; (iii) the quantum metric dipole (QMD) [51–53] and those revealed here as the 2nd-order skew scattering (2SK), 2nd-order side jump (2SJ), side-skew-scattering (SSK), Berry side jump (BSJ), and Berry skew scattering (BSK, part of it has been known as the anomalous skew scattering [45]) mechanisms, in the absence of  $\mathcal{T}$  and  $\mathcal{P}$  symmetries but under a joint  $\mathcal{PT}$  symmetry. The (i), (ii), and (iii) mechanisms can be roughly categorized by the power law of the scattering time  $\tau$ , i.e.,  $\tau^2$ ,  $\tau^1$ , and  $\tau^0$ , respectively.

may exhaust all possible mechanisms quadratic in electric field, i.e.,  $\propto E^2$ , as shown in Fig. 1(c).

Experimentally, the nonlinear Hall effect is measured as a double-frequency transverse voltage in response to a low-frequency current (10-1000 Hz). Theoretically, the nonlinear conductivity  $\chi_{abc}$  is defined in terms of the double-frequency current density

$$J_a(2\omega) = \chi_{abc} E_b(\omega) E_c(\omega), \quad (1)$$

in response to low-frequency electric fields  $E_b(\omega)$  and  $E_c(\omega)$ , where  $\omega$  is the frequency,  $a, b, c \in \{x, y, z\}$ .  $\chi_{abc}$  can be calculated using the semiclassical theory to treat geometry (i.e., Berry curvature) and disorder on an equal footing (see Appendix A). At the order of quantum metric, we find that the nonlinear conductivity  $\chi_{abc}$  can be decomposed as

$$\begin{aligned} \chi_{abc} = & \chi^{2\text{SK}} + \chi^{2\text{SJ}} + \chi^{\text{SSK}} + \chi^{\text{BSJ}} + \chi_2^{\text{BSK}} \\ & + \chi_1^{\text{BSK}} + \chi^{\text{Drude}} + \chi^{\text{QMD}}, \end{aligned} \quad (2)$$

where the first 5 mechanisms are our findings, in addition to the rest 3 known mechanisms, with their explicit forms given in Tab. IV. The hierarchy of all mechanisms for the nonlinear Hall effect is categorized in Fig. 1(c) according to three different symmetries. In particular, the  $\chi^{\text{QMD}}$  mechanism is important due to its dependence on the quantum metric dipole (QMD), the real part of the quantum geometry that measures the distance between quantum states (see Appendix B). The quantum metric has been found to play critical roles in the fractional Chern insulator and flat-band superconductivity, and thus has attracted tremendous interest [59–64, 68]. More importantly, all terms in Eq. (2) can survive under the same symmetry that the quantum metric emerges in

the nonlinear transport, specifically, the absence of time-reversal ( $\mathcal{T}$ ) and inversion ( $\mathcal{P}$ ) symmetries but under a joint  $\mathcal{PT}$  symmetry (see Appendix C).

*Scaling law at the order of quantum metric.*— Scaling law is the relation between the longitudinal conductivity and transverse conductivities. Scaling laws can distinguish the mechanisms in the previous Hall effects [6, 9, 15, 17, 69, 72, 73]. With the formulas in Tab. IV, we derive the scaling law at the order of quantum metric (Sec. SV of [74]), as a relation between the transverse nonlinear Hall conductivity  $\chi_{yxx}$  and longitudinal linear conductivity  $\sigma_{xx}$

$$\chi_{yxx} = \mathcal{C}_4 \sigma_{xx}^4 + \mathcal{C}_3 \sigma_{xx}^3 + \mathcal{C}_2 \sigma_{xx}^2 + \mathcal{C}_1 \sigma_{xx} + \mathcal{C}_0, \quad (3)$$

where in experiments  $\chi_{yxx} = [V_y^{2\omega} \sigma_{xx} / (V_x^\omega)^2] (L^2/W)$ ,  $L$  is the length,  $W$  is the width in 2D or cross-sectional area in 3D,  $V_y^{2\omega}$  is the transverse double-frequency voltage, and  $V_x^\omega$  is the longitudinal single-frequency voltage. The parameters  $\mathcal{C}_i$  are related to the mechanisms in Fig. 1, as shown in Tab. I.

TABLE I. Dependence of the parameters  $\mathcal{C}_i$  in the scaling law Eq. (3) on the mechanisms in Fig. 1. Details in Appendix E.

Parameters	Mechanisms
$\mathcal{C}_4 (\text{mA}^{-3} \cdot \text{nm} \cdot \text{V}^2)$	2SK
$\mathcal{C}_3 (\text{mA}^{-2} \cdot \text{nm} \cdot \text{V})$	2SK, SSK
$\mathcal{C}_2 (\text{mA}^{-1} \cdot \text{nm})$	2SK, SSK, 2SJ, BSK, Drude
$\mathcal{C}_1 (\text{nm} \cdot \text{V}^{-1})$	2SK, SSK, 2SJ, BSK, BJS
$\mathcal{C}_0 (\text{mA} \cdot \text{nm} \cdot \text{V}^{-2})$	2SK, SSK, 2SJ, BSK, BJS, QMD

In Fig. 2(a), we fit the experimental data of the 6-septuple-layer  $\text{MnBi}_2\text{Te}_4$  thin films strained by black phosphorus [54] with Eq. (3). The fitting can determine the weights of the five  $\mathcal{C}_i \sigma_{xx}^i$  terms in Eq. (3), as shown

in Fig. 2(b), which indicates that the  $\mathcal{C}_0$  term is dominant. According to Tab. I,  $\mathcal{C}_0$  differs from  $\mathcal{C}_1$  only by the QMD mechanism, indicating that the quantum metric is the dominant mechanism in this experiment. In contrast, Figs. 2(c) and 2(d) show that in 4-septuple-layer MnBi<sub>2</sub>Te<sub>4</sub> [55] the  $\mathcal{C}_4\sigma_{xx}^4$  term is comparable with other four  $\mathcal{C}_i\sigma_{xx}^i$  terms, meanwhile only the 2SK mechanism contributes to the  $\mathcal{C}_4\sigma_{xx}^4$  term according to Tab. I, implying the dominance of the 2nd-order skew scattering in this experiment. Following this clue, we further find that all five terms in Fig. 2(d) have the ratio  $\mathcal{C}_4\sigma_{xx}^4 : \mathcal{C}_3\sigma_{xx}^3 : \mathcal{C}_2\sigma_{xx}^2 : \mathcal{C}_1\sigma_{xx} : \mathcal{C}_0 = 0.853 : -3.56 : 5.57 : -3.87 : 1$ , roughly consistent with the ratio of coefficients

$$1 : -4 : 6 : -4 : 1 \quad (4)$$

in front of the parameter  $\mathcal{C}_{1111}^{2\text{SK}}$  in Eq. (E1), where each “1” in “1111” means a correlation between two dynamic scattering events (e.g., by phonons). More precisely, we calculate the ratio of the  $\mathcal{C}_{1111}^{2\text{SK}}$  terms according to Eq. (E1) as  $\sigma_{xx}^4/\sigma_{xx0}^4 : -4\sigma_{xx}^3/\sigma_{xx0}^3 : 6\sigma_{xx}^2/\sigma_{xx0}^2 : -4\sigma_{xx}/\sigma_{xx0} : 1 = 0.698 : -3.05 : 5.01 : -3.66 : 1$ , where  $\sigma_{xx0} = 186 \mu\text{S}$ , is the longitudinal linear conductivity at zero temperature (or the lowest temperature), and  $\sigma_{xx} = 170 \mu\text{S}$ , is taken at the middle of the temperature range, within the temperature range of 2-10 K in [55]. The above consistency in the ratio between the experiment and our theory indicates that the dominant mechanism in the 4-septuple-layer MnBi<sub>2</sub>Te<sub>4</sub> [55] is the 2nd-order skew scattering. Also, now the different signs and weights in Fig. 2(d) can be theoretically understood from the expansion of  $(\sigma_{xx}^{-1} - \sigma_{xx0}^{-1})^4$  in the derivation of the scaling law. A similar scaling law is found [75] but without giving the conductivity formulas or applied to experiments.

*Symmetry and Nonzero nonlinear conductivity elements.*— The quite different dominant mechanisms in the two experiments can be understood from symmetry. The unstrained MnBi<sub>2</sub>Te<sub>4</sub> thin film [55] has a three-fold rotational  $C_3$  symmetry but strained thin film [54] does not. On the other hand, the mechanisms at the order of quantum metric are classified into three types, according to their different symmetries (Sec. SIIIB of [74])

$$\begin{aligned} \text{2SK, 2SJ, SSK} : \chi_{abc} &= \chi_{acb}, \\ \text{QMD, BSJ, BSK} : \chi_{abc} &= -\chi_{cba}, \\ \text{Drude} : \chi_{abc} &= \chi_{bca} = \chi_{cab}, \end{aligned} \quad (5)$$

where  $\{a, b, c\} \in \{x, y, z\}$ . The  $C_3$  symmetry forbids  $\chi_{abc} = -\chi_{cba}$  [10], so the unstrained MnBi<sub>2</sub>Te<sub>4</sub> thin film [55] has no QMD contribution. By using strain to break the  $C_3$  symmetry, a finite  $\chi_{yxx}$  can be recovered, as those in the strained MnBi<sub>2</sub>Te<sub>4</sub> thin film [54].

Furthermore, we can generalize the symmetry properties to determine the nonzero nonlinear conductivity elements  $\chi_{abc}$  for all the crystals classified by the magnetic point groups, as shown in Tab. II for 2D cases. The

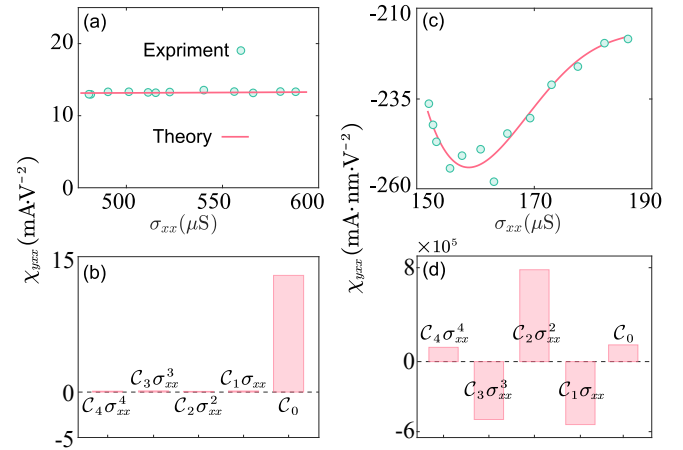


FIG. 2. (a) Scaling laws between the nonlinear Hall conductivity  $\chi_{yxx}$  and linear longitudinal conductivity  $\sigma_{xx}$  for the experimental data (circles) of the BP-6SL MnBi<sub>2</sub>Te<sub>4</sub> thin films (SL for septuple layer, BP for black phosphorous) [54], fitted by using Eq. (3) (solid curve). (b) Weights of the five  $\mathcal{C}_i\sigma_{xx}^i$  terms in Eq. (3) for the data from (a) at  $\sigma_{xx} = 540 \mu\text{S}$ . [(c) and (d)] The same as (a) and (b) except for the 4SL MnBi<sub>2</sub>Te<sub>4</sub> thin films [55] and  $\sigma_{xx} = 170 \mu\text{S}$  in (d). The fitting parameters in (a)  $\mathcal{C}_4 = 1.02 \times 10^{-12} \text{ mA}\cdot\text{V}^{-2}\cdot\mu\text{S}^{-4}$ ,  $\mathcal{C}_3 = 5.98 \times 10^{-10} \text{ mA}\cdot\text{V}^{-2}\cdot\mu\text{S}^{-3}$ ,  $\mathcal{C}_2 = 2.15 \times 10^{-7} \text{ mA}\cdot\text{V}^{-2}\cdot\mu\text{S}^{-2}$ ,  $\mathcal{C}_1 = 1.68 \times 10^{-4} \text{ mA}\cdot\text{V}^{-2}\cdot\mu\text{S}^{-1}$ ,  $\mathcal{C}_0 = 13.0 \text{ mA}\cdot\text{V}^{-2}$ , and in (c)  $\mathcal{C}_4 = 1.43 \times 10^{-4} \text{ mA}\cdot\text{nm}\cdot\text{V}^{-2}\cdot\mu\text{S}^{-4}$ ,  $\mathcal{C}_3 = -1.02 \times 10^{-1} \text{ mA}\cdot\text{nm}\cdot\text{V}^{-2}\cdot\mu\text{S}^{-3}$ ,  $\mathcal{C}_2 = 2.70 \times 10^1 \text{ mA}\cdot\text{nm}\cdot\text{V}^{-2}\cdot\mu\text{S}^{-2}$ ,  $\mathcal{C}_1 = -3.19 \times 10^3 \text{ mA}\cdot\text{nm}\cdot\text{V}^{-2}\cdot\mu\text{S}^{-1}$ ,  $\mathcal{C}_0 = 1.40 \times 10^5 \text{ mA}\cdot\text{nm}\cdot\text{V}^{-2}$ .

unstrained [55] and strained [54] MnBi<sub>2</sub>Te<sub>4</sub> thin films are classified in the  $\bar{3}'m'$  and  $2/m'$  magnetic point groups, respectively. Compared to the point groups, the magnetic point groups [76] can also describe the time-reversal symmetry breaking at the order of the quantum metric. Note that the QMD mechanism [77, 78] has fewer nonzero elements than the 2SK, 2SJ, and SSK mechanisms, because of the anti-symmetric constraint  $\chi_{abc} = -\chi_{cba}$ .

TABLE II. Nonzero nonlinear conductivity elements  $\chi_{abb}$  on the  $x$ - $y$  plane (defined as  $J_a = \chi_{abb}E_b^2$ ,  $\{a, b\} \in \{x, y\}$ ) for different mechanisms. In 2D, only 9 out of the 122 magnetic point groups [76] have nonzero elements. In 3D, 20 magnetic point groups have nonzero conductivity elements. More details in Sec. SIIIB of [74].

Groups	2SK/2SJ/SSK/Drude	QMD/BSJ/BSK
$\bar{1}', 2'/m$	$\chi_{xxx}$ $\chi_{yxx}$	$\chi_{yxx}$ $\chi_{xyy}$
$2/m', m'mm$	$\chi_{yxx}$ $\chi_{yyy}$	$\chi_{yxx}$
$\bar{3}'m, \bar{3}'m', 6'/mmm'$	$\chi_{yxx} = -\chi_{yyy}$	$\times$
$\bar{3}', 6'/m$	$\chi_{xyy} = -\chi_{xxx}$ $\chi_{yxx} = -\chi_{yyy}$	$\times$

*MnBi<sub>2</sub>Te<sub>4</sub> films and C<sub>3</sub> symmetry.*— To further verify the 2SK and QMD mechanisms in the MnBi<sub>2</sub>Te<sub>4</sub> thin films with and without the  $C_3$  symmetry [54, 55], we

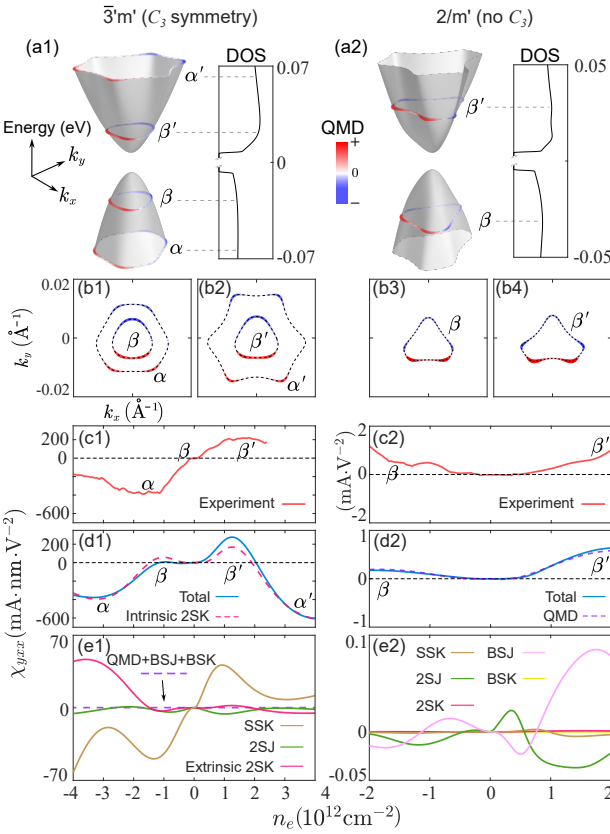


FIG. 3. For the model Eq. (6) of the even-layered  $\text{MnBi}_2\text{Te}_4$  thin films with and without the  $C_3$  symmetry (also classified by the  $\bar{3}'m'$  and  $2/m'$  magnetic point groups), [(a1) and (a2)] the energy bands and density of states (DOS), [(b1) and (b2)] the Fermi surfaces at the peaks and dips in (d1)-(d2), with the color bar featuring the distribution of the quantum metric dipole (QMD). [(c1) and (c2)] The measured nonlinear Hall conductivity  $\chi_{yxx}$  as a function of charge carrier density  $n_e$ , adapted from [55] (c1) and from [54] (c2), respectively. Only the data in (c2) is in 3D units. [(d1) and (d2)] The calculated nonlinear Hall conductivity from the intrinsic 2SK (d1) and QMD (d2) mechanisms, compared with the total nonlinear Hall conductivity in each case. The intrinsic and extrinsic 2SK contributions are defined in Tab. III. The Drude mechanism can be subtracted from the data [54] so is not included. [(e1) and (e2)] The splits of the others mechanisms.

calculate the nonlinear Hall conductivity by applying the formulas in Tab. IV to the minimal Hamiltonian of even-layered  $\text{MnBi}_2\text{Te}_4$  thin films

$$\hat{\mathcal{H}} = \hat{\mathcal{H}}_0 + \hat{\mathcal{H}}_S, \quad (6)$$

where  $\hat{\mathcal{H}}_0$  is for the  $C_3$  symmetric part [79] and  $\hat{\mathcal{H}}_S$  is for the  $C_3$ -symmetry-breaking part [54] (see Appendix D for explicit expressions). With and without  $\hat{\mathcal{H}}_S$ , the model is also classified into the  $2/m'$  and  $\bar{3}'/m'$  magnetic point groups, respectively. The energy bands and Fermi surfaces in Figs. 3 (a1)-(b4) show that the Hamiltonian can well describe the thin films with and without the  $C_3$  symmetry.

The calculated nonlinear Hall conductivities in Figs. 3(d1)-(e2) verify the dominance of the 2SK and QMD mechanisms in the presence and absence of the  $C_3$  symmetry, respectively. In addition, not only QMD but also the BSJ and BSK mechanisms vanish under the  $C_3$  symmetry and can be recovered by strain, consistent with the symmetry analysis. More importantly, the calculated nonlinear Hall conductivity can well capture the features in the experimental data, providing explanations for the complicated peaks and dips marked by  $\alpha$ ,  $\beta$ ,  $\alpha'$ , and  $\beta'$  in Figs. 3(c1)-(d2). They echo with the features in the energy bands, density of states (DOS), and quantum metric dipole (QMD) in Figs. 3(a1)-(b4). Specifically, as the Fermi surface changes from triangular to hexagonal, the density of states reaches a maximum, where both the 2SK and QMD mechanisms show peaks, as marked by  $\beta$  and  $\beta'$ . The difference is that the  $\beta$  peak of the 2SK mechanism is strongly suppressed by a broken particle-hole symmetry in the band structure and other mechanisms. As the Fermi surface completely turns hexagonal, the 2SK mechanism shows dips, as marked by  $\alpha$  and  $\alpha'$ . The 2SK mechanism shows similar  $\beta$  and  $\beta'$  peaks as those of the QMD mechanism because it is indeed the intrinsic part of the 2SK mechanism. Intrinsic means that it does not explicitly depend on the impurity density, although impurities are introduced in the calculation of the disorder-related mechanisms. Moreover, all the mechanisms in Tab. IV can be further classified by their dependence on the impurity density, as shown in Tab. III.

TABLE III. The dependence of the mechanisms on the impurity density  $n_i$ . The superscripts (3A) and (4A) indicate how many times the extrinsic skew scattering  $\varpi_{ll'}^{(3A)} \sim n_i V_1^3$  and intrinsic skew scattering  $\varpi_{ll'}^{(4A)} \sim (n_i V_0^2)^2$  [Eq. (A8)] appear in the formulas of  $\chi_{1,2}^{2\text{SK}}$  and  $\chi_{1,2,3,4}^{\text{SSK}}$ , where  $n_i V_0^2$  ( $n_i V_1^3$ ) measures the correlations of two (three) scattering events. The intrinsic and extrinsic 2SK contributions in Fig. 3 are  $\chi_{1,2}^{2\text{SK}(4A,4A)}$  and the rest of  $\chi_{1,2}^{2\text{SK}}$ , respectively.

Mechanisms	
$n_i^{-2}$	$\chi_{1,2}^{2\text{SK}(3A,3A)}, \chi^{\text{Drude}}$
$n_i^{-1}$	$\chi_1^{\text{BSK}}, \chi_{1,2}^{2\text{SK}(3A,4A)}, \chi_{1,2,3,4}^{\text{SSK}(3A)}$
$n_i^0$	$\chi_2^{\text{BSK}}, \chi_{1,2}^{\text{BSJ}}, \chi_{1,2,3}^{2\text{SJ}}, \chi_{1,2}^{2\text{SK}(4A,4A)}, \chi_{1,2,3,4}^{\text{SSK}(4A)}, \chi^{\text{QMD}}$

**Experimental implications.**—Our work can provide several potential future directions. The scaling law described in Eqs. (3), (E1), and Tab. I can be applied to identify mechanisms in future experiments on nonlinear transport. The nonzero elements of nonlinear conductivity in Tab. II can guide future experiments in more materials. The nonlinear conductivity formulas in Tab. IV can be applied to quantitatively study nonlinear transport in more systems with the  $\mathcal{PT}$  symmetry.

<sup>†</sup>Z. H. Gong and Z. Z. Du contributed equally. We thank helpful discussions with Xiangang Wan

and Xiaoqun Wang. This work was supported by the National Key R&D Program of China (2022YFA1403700), Innovation Program for Quantum Science and Technology (2021ZD0302400), the National Natural Science Foundation of China (11925402, 12374041, 12350402), Guangdong Basic and Applied Basic Research Foundation (2023B0303000011), Guangdong Provincial Quantum Science Strategic Initiative (GDZX2201001 and GDZX2401001), Guangdong province (2020KCXTD001), the Science, Technology and Innovation Commission of Shenzhen Municipality (ZDSYS20190902092905285), and Center for Computational Science and Engineering of SUSTech.

---

\* Corresponding author: luhz@sustech.edu.cn

[1] I. Sodemann and L. Fu, “Quantum nonlinear Hall effect induced by Berry curvature dipole in time-reversal invariant materials”, *Phys. Rev. Lett.* **115**, 216806 (2015).

[2] T. Low, Y. Jiang, and F. Guinea, “Topological currents in black phosphorus with broken inversion symmetry”, *Phys. Rev. B* **92**, 235447 (2015).

[3] Q. Ma, S.-Y. Xu, H. Shen, D. MacNeill, V. Fatemi, T.-R. Chang, *et al.*, “Observation of the nonlinear Hall effect under time-reversal-symmetric conditions”, *Nature* **565**, 337 (2019).

[4] Z. Z. Du, C. M. Wang, H.-Z. Lu, and X. C. Xie, “Band signatures for strong nonlinear Hall effect in bilayer WTe<sub>2</sub>”, *Phys. Rev. Lett.* **121**, 266601 (2018).

[5] K. Kang, T. Li, E. Sohn, J. Shan, and K. F. Mak, “Observation of the nonlinear anomalous Hall effect in few-layer WTe<sub>2</sub>”, *Nat. Mater.* **18**, 324 (2019).

[6] Z. Z. Du, C. M. Wang, S. Li, H.-Z. Lu, and X. C. Xie, “Disorder-induced nonlinear Hall effect with time-reversal symmetry”, *Nat. Commun.* **10**, 3047 (2019).

[7] S. Nandy and I. Sodemann, “Symmetry and quantum kinetics of the nonlinear Hall effect”, *Phys. Rev. B* **100**, 195117 (2019).

[8] C. Xiao, Z. Z. Du, and Q. Niu, “Theory of nonlinear Hall effects: Modified semiclassics from quantum kinetics”, *Phys. Rev. B* **100**, 165422 (2019).

[9] Z. Z. Du, H.-Z. Lu, and X. C. Xie, “Nonlinear Hall effects”, *Nat. Rev. Phys.* **3**, 744 (2021).

[10] Z. Z. Du, C. M. Wang, H.-P. Sun, H.-Z. Lu, and X. C. Xie, “Quantum theory of the nonlinear Hall effect”, *Nat. Commun.* **12**, 5038 (2021).

[11] S. Lai, H. Liu, Z. Zhang, J. Zhao, X. Feng, N. Wang, *et al.*, “Third-order nonlinear Hall effect induced by the Berry-connection polarizability tensor”, *Nat. Nanotechnol.* **16**, 869 (2021).

[12] S.-C. Ho, C.-H. Chang, Y.-C. Hsieh, S.-T. Lo, B. Huang, T.-H.-Y. Vu, C. Ortix, and T.-M. Chen, “Hall effects in artificially corrugated bilayer graphene without breaking time-reversal symmetry”, *Nat. Electron.* **4**, 116 (2021).

[13] P. He, H. Isobe, D. Zhu, C.-H. Hsu, L. Fu, and H. Yang, “Quantum frequency doubling in the topological insulator Bi<sub>2</sub>Se<sub>3</sub>”, *Nat. Commun.* **12**, 1 (2021).

[14] H. Watanabe and Y. Yanase, “Nonlinear electric transport in odd-parity magnetic multipole systems: Application to Mn-based compounds”, *Phys. Rev. Res.* **2**, 043081 (2020).

[15] A. Tiwari, F. Chen, S. Zhong, E. Drueke, J. Koo, A. Kaczmarek, *et al.*, “Giant c-axis nonlinear anomalous Hall effect in T<sub>d</sub>-MoTe<sub>2</sub> and WTe<sub>2</sub>”, *Nat. Commun.* **12**, 2049 (2021).

[16] E. J. König and A. Levchenko, “Quantum kinetics of anomalous and nonlinear Hall effects in topological semimetals”, *Ann. Phys.* **435**, 168492 (2021).

[17] J. Duan, Y. Jian, Y. Gao, H. Peng, J. Zhong, Q. Feng, J. Mao, and Y. Yao, “Giant second-order nonlinear Hall effect in twisted bilayer graphene”, *Phys. Rev. Lett.* **129**, 186801 (2022).

[18] P. He, G. K. W. Koon, H. Isobe, J. Y. Tan, J. Hu, A. H. C. Neto, L. Fu, and H. Yang, “Graphene moiré superlattices with giant quantum nonlinearity of chiral Bloch electrons”, *Nat. Nanotechnol.* **17**, 378 (2022).

[19] M. Huang, Z. Wu, J. Hu, X. Cai, E. Li, L. An, *et al.*, “Giant nonlinear Hall effect in twisted bilayer WSe<sub>2</sub>”, *Natl. Sci. Rev.* **10**, nwac232 (2022).

[20] S. Sinha, P. C. Adak, A. Chakraborty, K. Das, K. Debnath, L. V. Sangani, *et al.*, “Berry curvature dipole senses topological transition in a moiré superlattice”, *Nat. Phys.* **18**, 765 (2022).

[21] D. Kaplan, T. Holder, and B. Yan, “General nonlinear Hall current in magnetic insulators beyond the quantum anomalous Hall effect”, *Nat. Commun.* **14**, 3053 (2023).

[22] L. Min, H. Tan, Z. Xie, L. Miao, R. Zhang, S. H. Lee, *et al.*, “Strong room-temperature bulk nonlinear Hall effect in a spin-valley locked Dirac material”, *Nat. Commun.* **14**, 364 (2023).

[23] Z. Jin, X. Yao, Z. Wang, H. Y. Yuan, Z. Zeng, W. Wang, Y. Cao, and P. Yan, “Nonlinear topological magnon spin Hall effect”, *Phys. Rev. Lett.* **131**, 166704 (2023).

[24] T. Yokouchi, Y. Ikeda, T. Morimoto, and Y. Shiomi, “Giant magnetochiral anisotropy in Weyl semimetal WTe<sub>2</sub> induced by diverging Berry curvature”, *Phys. Rev. Lett.* **130**, 136301 (2023).

[25] M. Huang, Z. Wu, X. Zhang, X. Feng, Z. Zhou, S. Wang, *et al.*, “Intrinsic nonlinear Hall effect and gate-switchable Berry curvature sliding in twisted bilayer graphene”, *Phys. Rev. Lett.* **131**, 066301 (2023).

[26] M. Suárez-Rodríguez, B. Martín-García, W. Skowroński, F. Calavalle, S. S. Tsirkin, I. Souza, *et al.*, “Odd nonlinear conductivity under spatial inversion in chiral tellurium”, *Phys. Rev. Lett.* **132**, 046303 (2024).

[27] D. Kaplan, T. Holder, and B. Yan, “Unification of nonlinear anomalous Hall effect and nonreciprocal magnetoresistance in metals by the quantum geometry”, *Phys. Rev. Lett.* **132**, 026301 (2024).

[28] R. Chen, Z. Z. Du, H.-P. Sun, H.-Z. Lu, and X. C. Xie, “Nonlinear Hall effect on a disordered lattice”, *Phys. Rev. B* **110**, L081301 (2024).

[29] Y. D. Wang, Z. F. Zhang, Z.-G. Zhu, and G. Su, “Intrinsic nonlinear Ohmic current”, *Phys. Rev. B* **109**, 085419 (2024).

[30] L. Xiang and J. Wang, “Intrinsic in-plane magnetononlinear Hall effect in tilted Weyl semimetals”, *Phys. Rev. B* **109**, 075419 (2024).

[31] C. Chen, D. Zhai, C. Xiao, and W. Yao, “Crossed nonlinear dynamical Hall effect in twisted bilayers”, *Phys. Rev. Res.* **6**, L012059 (2024).

[32] J. Yao, Y. Liu, and W. Duan, “Geometrical nonlinear Hall effect induced by Lorentz force”, *Phys. Rev. B* **110**, 115123 (2024).

[33] P. He, H. Isobe, G. K. W. Koon, J. Y. Tan, J. Hu, J. Li, N. Nagaosa, and J. Shen, “Third-order nonlinear Hall effect in a quantum Hall system”, *Nat. Nanotechnol.* **(2024)**, 10.1038/s41565-024-01730-1.

[34] E. Wang, H. Zeng, W. Duan, and H. Huang, “Spontaneous inversion symmetry breaking and emergence of Berry curvature and orbital magnetization in topological ZrTe<sub>5</sub> films”, *Phys. Rev. Lett.* **132**, 266802 (2024).

[35] P. Makushko, S. Kovalev, Y. Zabila, I. Ilyakov, A. Ponomaryov, A. Arshad, *et al.*, “A tunable room-temperature nonlinear Hall effect in elemental bismuth thin films”, *Nat. Electron.* **7**, 207 (2024).

[36] J.-M. Lihm and C.-H. Park, “Nonlinear Hall effect from long-lived valley-polarizing relaxons”, *Phys. Rev. Lett.* **132**, 106402 (2024).

[37] H. Isobe, S.-Y. Xu, and L. Fu, “High-frequency rectification via chiral Bloch electrons”, *Sci. Adv.* **6**, eaay2497 (2020).

[38] D. Kumar, C.-H. Hsu, R. Sharma, T.-R. Chang, P. Yu, J. Wang, G. Eda, G. Liang, and H. Yang, “Room-temperature nonlinear Hall effect and wireless radiofrequency rectification in Weyl semimetal TaIrTe<sub>4</sub>”, *Nat. Nanotechnol.* **16**, 421 (2021).

[39] X. F. Lu, C.-P. Zhang, N. Wang, D. Zhao, X. Zhou, W. Gao, X. H. Chen, K. Law, and K. P. Loh, “Nonlinear transport and radio frequency rectification in BiTeBr at room temperature”, *Nat. Commun.* **15**, 245 (2024).

[40] J. Kim, K.-W. Kim, D. Shin, S.-H. Lee, J. Sinova, N. Park, and H. Jin, “Prediction of ferroelectricity-driven Berry curvature enabling charge- and spin-controllable photocurrent in tin telluride monolayers”, *Nat. Commun.* **10**, 3965 (2019).

[41] P. Bhalla, A. H. MacDonald, and D. Culcer, “Resonant photovoltaic effect in doped magnetic semiconductors”, *Phys. Rev. Lett.* **124**, 087402 (2020).

[42] Q. Ma, A. G. Grushin, and K. S. Burch, “Topology and geometry under the nonlinear electromagnetic spotlight”, *Nat. Mater.* **20**, 1601 (2021).

[43] P. J. D. Crowley and L. Fu, “Supercurrent-induced resonant optical response”, *Phys. Rev. B* **106**, 214526 (2022).

[44] A. Chotrattanapituk, M. Mandal, and M. Li, “Bridging the gap to THz optoelectronics with nonlinear Hall devices”, *Matter* **6**, 2514 (2023).

[45] D. Ma, A. Arora, G. Vignale, and J. C. W. Song, “Anomalous skew-scattering nonlinear Hall effect and chiral photocurrents in  $\mathcal{PT}$ -symmetric antiferromagnets”, *Phys. Rev. Lett.* **131**, 076601 (2023).

[46] H. Zhou, R.-C. Xiao, S.-H. Zhang, W. Gan, H. Han, H.-M. Zhao, *et al.*, “Skin effect of nonlinear optical responses in antiferromagnets”, *Phys. Rev. Lett.* **133**, 236903 (2024).

[47] B. Ghosh, Y. Onishi, S.-Y. Xu, H. Lin, L. Fu, and A. Bansil, “Probing quantum geometry through optical conductivity and magnetic circular dichroism”, *Sci. Adv.* **10**, eado1761 (2024).

[48] D. Shin, A. Rubio, and P. Tang, “Light-induced ideal Weyl semimetal in HgTe via nonlinear phononics”, *Phys. Rev. Lett.* **132**, 016603 (2024).

[49] Y. Shen, L. Primeau, J. Li, T.-D. Nguyen, D. Mandrus, Y. C. Lin, and Y. Zhang, “Nonlinear photocurrent in quantum materials for broadband photodetection”, *Prog. Quantum Electron.* **97**, 100535 (2024).

[50] D. Ma, Y. Xiong, and J. C. W. Song, “Metallic electro-optic effect in gapped bilayer graphene”, *Nano Lett.* **25**, 1260 (2025).

[51] Y. Gao, S. A. Yang, and Q. Niu, “Field induced positional shift of Bloch electrons and its dynamical implications”, *Phys. Rev. Lett.* **112**, 166601 (2014).

[52] C. Wang, Y. Gao, and D. Xiao, “Intrinsic nonlinear Hall effect in antiferromagnetic tetragonal CuMnAs”, *Phys. Rev. Lett.* **127**, 277201 (2021).

[53] H. Liu, J. Zhao, Y.-X. Huang, W. Wu, X.-L. Sheng, C. Xiao, and S. A. Yang, “Intrinsic second-order anomalous Hall effect and its application in compensated antiferromagnets”, *Phys. Rev. Lett.* **127**, 277202 (2021).

[54] A. Gao, Y.-F. Liu, J.-X. Qiu, B. Ghosh, T. V. Trevisan, Y. Onishi, *et al.*, “Quantum metric nonlinear Hall effect in a topological antiferromagnetic heterostructure”, *Science* **381**, 181 (2023).

[55] N. Wang, D. Kaplan, Z. Zhang, T. Holder, N. Cao, A. Wang, *et al.*, “Quantum-metric-induced nonlinear transport in a topological antiferromagnet”, *Nature* **621**, 487 (2023).

[56] Y. Fang, J. Cano, and S. A. A. Ghorashi, “Quantum geometry induced nonlinear transport in altermagnets”, *Phys. Rev. Lett.* **133**, 106701 (2024).

[57] J. Provost and G. Vallee, “Riemannian structure on manifolds of quantum states”, *Commun. Math. Phys.* **76**, 289 (1980).

[58] R. Resta, “The insulating state of matter: a geometrical theory”, *Eur. Phys. J. B* **79**, 121 (2011).

[59] S. A. Parameswaran, R. Roy, and S. L. Sondhi, “Fractional Chern insulators and the  $W_\infty$  algebra”, *Phys Rev B* **85**, 241308 (2012).

[60] R. Roy, “Band geometry of fractional topological insulators”, *Phys Rev B* **90**, 165139 (2014).

[61] T. S. Jackson, G. Möller, and R. Roy, “Geometric stability of topological lattice phases”, *Nat Commun* **6**, 8629 (2015).

[62] S. Peotta and P. Törmä, “Superfluidity in topologically nontrivial flat bands”, *Nat Commun* **6**, 8944 (2015).

[63] P. Törmä, S. Peotta, and B. A. Bernevig, “Superconductivity, superfluidity and quantum geometry in twisted multilayer systems”, *Nat. Rev. Phys.* **4**, 528 (2022).

[64] P. Törmä, “Essay: Where can quantum geometry lead us?”, *Phys. Rev. Lett.* **131**, 240001 (2023).

[65] B. Hetényi and P. Lévay, “Fluctuations, uncertainty relations, and the geometry of quantum state manifolds”, *Phys. Rev. A* **108**, 032218 (2023).

[66] A. Bouhon, A. Timmel, and R.-J. Slager, “Quantum geometry beyond projective single bands”, *arXiv:2303.02180* (2023).

[67] J. Hu, W. Li, H. Wang, and K. Chang, “Phonon-mediated nonlinear optical responses and quantum geometry”, *arXiv:2410.09677* (2024).

[68] T. Liu, X.-B. Qiang, H.-Z. Lu, and X. C. Xie, “Quantum geometry in condensed matter”, *Natl. Sci. Rev.* , nwae334 (2024).

[69] N. Nagaosa, J. Sinova, S. Onoda, A. H. MacDonald, and N. P. Ong, “Anomalous Hall effect”, *Rev. Mod. Phys.* **82**, 1539 (2010).

[70] R. B. Atencia, D. Xiao, and D. Culcer, “Disorder in the nonlinear anomalous Hall effect of  $\mathcal{PT}$ -symmetric Dirac fermions”, *Phys. Rev. B* **108**, L201115 (2023).

[71] D. Xiao, M. C. Chang, and Q. Niu, “Berry phase effects on electronic properties”, *Rev. Mod. Phys.* **82**, 1959 (2010).

[72] Y. Tian, L. Ye, and X. Jin, “Proper scaling of the anomalous Hall effect in topological insulators”, *Phys. Rev. B* **108**, 115111 (2023).

lous Hall effect”, *Phys. Rev. Lett.* **103**, 087206 (2009).

[73] D. Hou, G. Su, Y. Tian, X. Jin, S. A. Yang, and Q. Niu, “Multivariable scaling for the anomalous Hall effect”, *Phys. Rev. Lett.* **114**, 217203 (2015).

[74] See Supplemental Materials for the detailed calculations.

[75] Y.-X. Huang, C. Xiao, S. A. Yang, and X. Li, “Scaling law for time-reversal-odd nonlinear transport”, [arXiv:2311.01219](https://arxiv.org/abs/2311.01219) (2023).

[76] “Magnetic point group”, [https://en.wikipedia.org/wiki/Magnetic\\_space\\_group](https://en.wikipedia.org/wiki/Magnetic_space_group).

[77] Z.-F. Zhang, Z.-G. Zhu, and G. Su, “Symmetry dictionary on charge and spin nonlinear responses for all magnetic point groups with nontrivial topological nature”, *Natl. Sci. Rev.* **10**, nwad104 (2023).

[78] H. Zhu, J. Li, X. Chen, Y. Yu, and Q. Liu, “Magnetic geometry to quantum geometry nonlinear transports”, [arXiv:2406.03738](https://arxiv.org/abs/2406.03738) (2024).

[79] H.-P. Sun, C. M. Wang, S.-B. Zhang, R. Chen, Y. Zhao, C. Liu, Q. Liu, C. Chen, H.-Z. Lu, and X. C. Xie, “Analytical solution for the surface states of the antiferromagnetic topological insulator  $\text{MnBi}_2\text{Te}_4$ ”, *Phys. Rev. B* **102**, 241406 (2020).

[80] N. A. Sinitsyn, “Semiclassical theories of the anomalous Hall effect”, *J. Phys. Condens. Matter* **20**, 023201 (2008).

[81] G. D. Mahan, *Many-Particle Physics* (Plenum Press, 1990).

[82] R. B. Atencia, Q. Niu, and D. Culcer, “Semiclassical response of disordered conductors: Extrinsic carrier velocity and spin and field-corrected collision integral”, *Phys. Rev. Res.* **4**, 013001 (2022).

[83] H. Liu, J. H. Cullen, and D. Culcer, “Topological nature of the proper spin current and the spin-Hall torque”, *Phys. Rev. B* **108**, 195434 (2023).

[84] M. Mehraeen, “Quantum kinetic theory of quadratic responses”, *Phys. Rev. B* **110**, 174423 (2024).

## End Matter

*Appendix A: Derivation of nonlinear conductivity formulas.* We briefly describe the calculation of the nonlinear conductivity formulas (details in Secs. SI and SII of [74]). We start with the uniform Boltzmann equation [6, 80]

$$\partial f_l / \partial t + \dot{\mathbf{k}} \cdot \partial f_l / \partial \mathbf{k} = \mathcal{I}_{el}\{f_l\} \quad (\text{A1})$$

of the distribution function  $f_l$ , where  $\mathcal{I}_{el}\{f_l\}$  accounts for the elastic disorder scattering,  $l$  stands for the band index  $\gamma$  and wave vector  $\mathbf{k}$ ,  $\dot{\mathbf{k}} = -(e/\hbar)\mathbf{E}$ , and  $\mathbf{E}$  is the electric field. By decoupling the distribution function and scattering according to different mechanisms (*in* for disorder-irrelevant,  $sj$  and  $sk$  for side jump and skew scattering, respectively)

$$\begin{aligned} f_l &= f_l^{in} + \delta f_l^{sj} + \delta f_l^{sk} + \delta f_l^{2sj} + \delta f_l^{2sk} + \delta f_l^{sk,sj}, \\ \mathcal{I}_{el}\{f_l\} &= \mathcal{I}^{in} + \mathcal{I}^{sj} + \mathcal{I}^{sk} + \mathcal{I}^{sk,sj}, \end{aligned} \quad (\text{A2})$$

$f_l$  can be found up to the second order of  $\mathbf{E}$ , where  $\delta f_l^{2sj} + \delta f_l^{2sk} + \delta f_l^{sk,sj}$  and  $\mathcal{I}^{sk,sj}$  are crucial for new findings. The nonlinear conductivity  $\chi_{abc}$  can be extracted from the electric current density  $\mathbf{J}(\mathbf{E}) = -e \sum_l \dot{\mathbf{r}}_l f_l$ , where the velocity

$$\dot{\mathbf{r}}_l = \mathbf{v}_l - \dot{\mathbf{k}} \times (\boldsymbol{\Omega}_l + \nabla_{\mathbf{k}} \times \mathbf{G}\mathbf{E}) + \mathbf{v}_l^{sj} \quad (\text{A3})$$

includes the terms from the group velocity  $\mathbf{v}_l$ , Berry curvature  $\boldsymbol{\Omega}$  [71], Berry connection polarizability  $\mathbf{G}$ , and side-jump velocity  $\mathbf{v}^{sj}$ .

The the nonlinear conductivity formula at the order of quantum metric in Eq. (2) can be decomposed into

$$\begin{aligned} \chi_{abc} &= \sum_{i=1}^2 \chi_i^{2\text{SK}} + \sum_{i=1}^3 \chi_i^{2\text{SJ}} + \sum_{i=1}^4 \chi_i^{\text{SSK}} + \chi^{\text{BSJ}} + \chi_2^{\text{BSK}} \\ &\quad + \chi_1^{\text{BSK}} + \chi^{\text{Drude}} + \chi^{\text{QMD}}. \end{aligned} \quad (\text{A4})$$

Their explicit forms are given in Tab. IV, where  $-e$  is the electron charge, the scattering time  $\tau$  is defined as (Sec. SIB of [74])

$$\frac{1}{\tau} \approx \frac{1}{\tau_{\mathbf{k}}} \equiv \sum_{\mathbf{k}'} \varpi_{\mathbf{k}'\mathbf{k}'}^{(2)} [1 - \cos(\phi - \phi')] \delta(\epsilon_F - \epsilon_l), \quad (\text{A5})$$

$\varepsilon^{abc}$  is the anti-symmetric tensor, the Fermi distribution  $f_l^{(0)} = \{\exp[(\epsilon_l - \epsilon_F)/k_B T] + 1\}^{-1}$ , with the Fermi energy  $\epsilon_F$ ,  $l$  stands for  $(\gamma, \mathbf{k})$ , with the band index  $\gamma$  and wave vector  $\mathbf{k} = |k|(\cos\phi, \sin\phi)$  in 2D, the Berry curvature [71]

$$\Omega_l^a \equiv -2\varepsilon^{abc} \sum_{\gamma' \neq \gamma} \frac{\text{Im}(\gamma | \partial_{\mathbf{k}}^b \hat{\mathcal{H}} | \gamma') \langle \gamma' | \partial_{\mathbf{k}}^c \hat{\mathcal{H}} | \gamma \rangle}{(\epsilon_{\mathbf{k}}^{\gamma} - \epsilon_{\mathbf{k}}^{\gamma'})^2}, \quad (\text{A6})$$

$\partial_{\mathbf{k}}^b \equiv \partial/\partial k_b$ ,  $\hat{\mathcal{H}}$  is the Hamiltonian,  $\epsilon_l$  is the eigen energy, group velocity  $v_l^a = (1/\hbar)\partial\epsilon_l/\partial k_a$ ,  $\partial_{\epsilon_l} \equiv \partial/\partial\epsilon_l$ ,

TABLE IV. Formulas of the nonlinear conductivity at the order of quantum metric, including the quantum metric dipole (QMD), Drude, mixed Berry curvature and skew scattering (BSK), mixed Berry curvature and side jump (BSJ), second-order side jump (2SJ) and skew scattering (2SK), mixed side jump and skew scattering (SSK). The hierarchy and physical pictures of them are illustrated in Fig. 1. The quantities and symbols are defined below Eq. (A4).

$$\begin{aligned} \chi^{\text{QMD}} &= e^2 \sum_l (v_l^a \mathcal{G}_l^{bc} - v_l^b \mathcal{G}_l^{ac}) \partial_{\epsilon_l} f_l^{(0)} [51-53], \\ \chi^{\text{Drude}} &= -\frac{\tau^2 e^3}{2\hbar^2} \sum_l v_l^a \partial_{\mathbf{k}}^b \partial_{\mathbf{k}}^c f_l^{(0)} [1], \\ \chi_1^{\text{BSK}} &= \frac{\tau^2 e^3}{2\hbar^2} \sum_{ll'} \varepsilon^{acd} \Omega_{l'}^d \varpi_{ll'}^{(3A)} \partial_{\mathbf{k}}^b f_l^{(0)} [45], \\ \chi_2^{\text{BSK}} &= \frac{\tau^2 e^3}{2\hbar^2} \sum_{ll'} \varepsilon^{acd} \Omega_{l'}^d \varpi_{ll'}^{(4A)} \partial_{\mathbf{k}}^b f_l^{(0)}, \\ \chi^{\text{BSJ}} &= \frac{\tau^2 e^3}{2\hbar^2} \sum_l \varepsilon^{acd} \Omega_{l'}^d v_l^{sj,b} \partial_{\epsilon_l} f_l^{(0)}, \\ \chi_1^{\text{2SK}} &= \frac{e^3}{2\hbar^4} \sum_{ll'} (v_{l''}^c v_{l''}^a) \varpi_{ll'}^A \varpi_{ll'}^A \partial_{\mathbf{k}}^b f_l^{(0)}, \\ \chi_2^{\text{2SK}} &= \frac{e^3}{2\hbar^4} \sum_{ll'} v_{l''}^a (\partial_{\mathbf{k}}^c - \partial_{\mathbf{k}}^l) \varpi_{ll'}^A \varpi_{ll'}^A \partial_{\mathbf{k}}^b f_l^{(0)}, \\ \chi_1^{\text{2SJ}} &= \frac{\tau^2 e^3}{2\hbar^2} \sum_{ll'} (v_{l'}^a + v_l^a) \bar{\Omega}_{ll'}^c v_l^{sj,b} \partial_{\epsilon_l} f_l^{(0)}, \\ \chi_2^{\text{2SJ}} &= \frac{\tau^2 e^3}{2\hbar^2} \sum_{ll'} (v_l^{sj,a} + v_{l'}^{sj,a}) \bar{\Omega}_{ll'}^c \partial_{\mathbf{k}}^b f_l^{(0)}, \\ \chi_3^{\text{2SJ}} &= -\frac{\tau^2 e^3}{2\hbar^2} \sum_l \partial_{\mathbf{k}}^b v_l^{sj,a} v_l^{sj,c} \partial_{\epsilon_l} f_l^{(0)}, \\ \chi_1^{\text{SSK}} &= \frac{\tau^2 e^3}{2\hbar^2} \sum_{ll'} (v_l^a + v_{l'}^a) \bar{\Omega}_{ll'}^c \partial_{\mathbf{k}}^b f_l^{(0)}, \\ \chi_2^{\text{SSK}} &= \frac{\tau^2 e^3}{2\hbar^2} \sum_{ll'} (v_{l''}^a + v_l^a) \varpi_{ll'}^A \bar{\Omega}_{ll'}^c \partial_{\mathbf{k}}^b f_l^{(0)}, \\ \chi_3^{\text{SSK}} &= \frac{\tau^2 e^3}{2\hbar^2} \sum_{ll'} (v_{l''}^a + v_{l''}^a) (\varpi_{ll'}^A + \varpi_{ll'}^A) v_{l'}^a \bar{\Omega}_{ll'}^c \partial_{\mathbf{k}}^b f_l^{(0)} \\ &\quad + \frac{\tau^3 e^3}{2\hbar^2} \sum_{ll'} v_{l'}^a v_l^{sj,b} (\partial_{\mathbf{k}}^c - \partial_{\mathbf{k}}^l) \varpi_{ll'}^A \partial_{\epsilon_l} f_l^{(0)}, \\ \chi_4^{\text{SSK}} &= \frac{\tau^2 e^3}{2\hbar^2} \sum_{ll'} v_{l'}^{sj,a} (\partial_{\mathbf{k}}^c - \partial_{\mathbf{k}}^l) \varpi_{ll'}^A \partial_{\mathbf{k}}^b f_l^{(0)}. \end{aligned}$$

$\partial_{\epsilon_l} f_l^{(0)}$  means summing those states near the Fermi surface. The side-jump velocity  $v_l^{sj,a} = \sum_{l'} \varpi_{ll'}^S \delta r_{ll'}^a$ ,  $\varpi_{ll'}^S$  ( $\varpi_{ll'}^A$ ) is the symmetric (anti-symmetric) scattering rate between states  $l$  and  $l'$ , the coordinates shift

$$\delta r_{ll'}^a \equiv i \langle l | \partial_{\mathbf{k}}^a | l' \rangle - i \langle l' | \partial_{\mathbf{k}}^a | l' \rangle - (\partial_{\mathbf{k}}^a + \partial_{\mathbf{k}'}^a) \arg(V_{ll'}), \quad (\text{A7})$$

with  $V_{ll'} = \langle l | \hat{V}_{imp} | l' \rangle$  [6, 80], where the  $\delta$ -correlated random potential  $\hat{V}_{imp}(\mathbf{r}) = \sum_i V_i \delta(\mathbf{r} - \mathbf{R}_i)$  can give the Gaussian  $\langle V_i^2 \rangle_{dis} = V_0^2$ , and non-Gaussian correlations  $\langle V_i^3 \rangle_{dis} = V_0^3$  [6, 10, 80], leading to the intrinsic skew scattering  $\varpi_{ll'}^{(4A)}$  and extrinsic skew scattering  $\varpi_{ll'}^{(3A)}$  parts to

$$\varpi_{ll'}^A = \varpi_{ll'}^{3A} + \varpi_{ll'}^{4A}. \quad (\text{A8})$$

$\bar{\Omega}_{ll'}^a$  ( $\bar{\Omega}_{ll'}^a$ ) is the symmetric (anti-symmetric) part of [6]

$$O_{ll'}^a \equiv (2\pi/\hbar) |T_{ll'}|^2 \delta r_{ll'}^a \partial_{\epsilon_l} \delta(\epsilon_l - \epsilon_{l'}), \quad (\text{A9})$$

and  $T_{ll'}$  is the T-matrix [81]. Alternatively, the calculation can be based on the density matrix [70, 82-84].

*Appendix B: Nonlinear conductivity of quantum metric dipole.* In the nonlinear conductivity formula of the quantum metric dipole mechanism  $\chi^{\text{QMD}}$  in Tab. IV, the Berry connection polarizability tensor reads [51-53]

$$G_{\gamma,\mathbf{k}}^{ab} \equiv 2e \text{Re} \sum_{\gamma' \neq \gamma} A_{a,\mathbf{k}}^{\gamma\gamma'} A_{b,\mathbf{k}}^{\gamma'\gamma} / (\epsilon_{\mathbf{k}}^{\gamma} - \epsilon_{\mathbf{k}}^{\gamma'}) \quad (\text{B1})$$

is related to the quantum metric tensor [57, 58]

$$g_{\gamma,\mathbf{k}}^{ab} \equiv \text{Re} \sum_{\gamma' \neq \gamma} A_{a,\mathbf{k}}^{\gamma\gamma'} A_{b,\mathbf{k}}^{\gamma'\gamma}, \quad (\text{B2})$$

where the Berry connection  $A_{a,\mathbf{k}}^{\gamma\gamma'} \equiv i\langle\gamma|\partial_{\mathbf{k}}^a|\gamma'\rangle$  [71]. For two-band systems, they are explicitly related as

$$\mathcal{G}_{\gamma,\mathbf{k}}^{ab} = 2eg_{\gamma,\mathbf{k}}^{ab}/(\epsilon_{\mathbf{k}}^{\gamma} - \epsilon_{\mathbf{k}}^{\gamma'}). \quad (\text{B3})$$

**Appendix C: Symmetry of nonlinear conductivity formulas.** In Eq. (B1), the velocity  $v$  is odd under both time-reversal ( $\mathcal{T}$ ) and inversion ( $\mathcal{P}$ ) operations, while the Berry curvature polarizability  $\mathcal{G}$  is even under both  $\mathcal{T}$  and  $\mathcal{P}$  operations, so  $v\mathcal{G}$  is odd under both  $\mathcal{T}$  and  $\mathcal{P}$  operations but even under the joint  $\mathcal{PT}$  symmetry. Therefore, to have a nonzero  $\chi^{\text{QMD}}$ , both the  $\mathcal{T}$  and  $\mathcal{P}$  must be broken, while  $\chi^{\text{QMD}}$  can survive the  $\mathcal{PT}$  symmetry. We can use Tab. V to check that all formulas in Tab. IV have the same symmetries of  $\chi^{\text{QMD}}$ .

TABLE V. Whether the quantities in the nonlinear conductivity formulas in Tab. IV change sign (+) or not (-), under inversion  $\mathcal{P}$ , time-reversal  $\mathcal{T}$ , and the joint  $\mathcal{PT}$  symmetry operations.

	$\partial_a$	$v_l^a$	$\Omega_l^a$	$\delta r_{ll'}^a$	$v_{a,l}^{sj}$	$\bar{O}_{ll'}^a$	$\bar{O}_{ll'}^a$	$\varpi_{ll'}^S$	$\varpi_{ll'}^A$
$\mathcal{P}$	-	-	+	-	-	-	-	+	+
$\mathcal{T}$	-	-	-	+	+	+	-	+	-
$\mathcal{PT}$	+	+	-	-	-	-	+	+	-

Take the formula of  $\chi_4^{\text{SSK}}$  in Tab. IV for example, in which  $v_{l'}^{sj,a}(\partial_{\mathbf{k}}^c - \partial_{\mathbf{k}}^c)\varpi_{ll'}^A\partial_{\mathbf{k}}^b$  gives  $(-1)(-1)(+1)(-1) = -1$  upon inversion,  $(+1)(-1)(-1)(-1) = -1$  upon time-reversal, and  $(-1)(+1)(-1)(+1) = 1$  under the joint  $\mathcal{PT}$  operation, so it has the same symmetry of  $\chi^{\text{QMD}}$ . The symmetry of the other formulas can be shown similarly (Sec. SIII of [74]).

**Appendix D: Hamiltonian for even-layer  $\text{MnBi}_2\text{Te}_4$  films.** In Eq. (6), the Hamiltonian for  $\text{MnBi}_2\text{Te}_4$  films with the  $C_3$  symmetry reads [79]

$$\hat{\mathcal{H}}_0 = \begin{pmatrix} h_0 + h_k & i\gamma k_- & m_k & 0 \\ -i\gamma k_+ & h_0 - h_k & 0 & -m_k \\ m_k & 0 & h_0 - h_k & i\gamma k_- \\ 0 & -m_k & -i\gamma k_+ & h_0 + h_k \end{pmatrix}, \quad (\text{D1})$$

where  $h_0 = E_0 - Dk^2$ ,  $k_x$  and  $k_y$  are wave vectors,  $k_{\pm} \equiv k_x \pm ik_y$ ,  $k^2 \equiv k_x^2 + k_y^2$ ,  $h_k = \Delta/2 - Bk^2$ ,  $m_k = m_2 + \beta_1(3k_x^2k_y - k_y^3)$ ,  $E_0$ ,  $D$ ,  $\Delta$ ,  $B$ ,  $m_2$ ,  $\beta_1$ , and  $\gamma$  are model parameters. The  $C_3$ -symmetry-breaking part reads [54]

$$\hat{\mathcal{H}}_S = \begin{pmatrix} s_1 k_y^2 & & h.c. & \\ -is_5 k_y & s_3 k_y^2 & & \\ s_7 k_y - is_8 k_x & 0 & s_3 k_y^2 & \\ 0 & -s_7 k_y + is_8 k_x & -is_5 k_y & s_1 k_y^2 \end{pmatrix}, \quad (\text{D2})$$

where  $s_1$ ,  $s_3$ ,  $s_5$ ,  $s_7$ , and  $s_8$  are model parameters. For BP-6SL  $\text{MnBi}_2\text{Te}_4$ , the parameters are  $\gamma = -3.1964 \text{ eV}\cdot\text{\AA}$ ,  $E_0 = 0 \text{ eV}$ ,  $D = 30 \text{ eV}\cdot\text{\AA}^2$ ,  $\Delta = 9.21 \text{ meV}$ ,  $B = 50 \text{ eV}\cdot\text{\AA}^2$ ,  $m_2 = -27.3 \text{ meV}$ ,  $\beta_1 = -12000 \text{ eV}\cdot\text{\AA}^3$ ,  $s_1 = 20 \text{ eV}\cdot\text{\AA}^2$ ,  $s_3 = 20 \text{ eV}\cdot\text{\AA}^2$ ,  $s_5 = -0.2 \text{ eV}\cdot\text{\AA}$ ,  $s_7 = -0.5 \text{ eV}\cdot\text{\AA}$ ,  $s_8 = -0.2 \text{ eV}\cdot\text{\AA}$ . For 4SL  $\text{MnBi}_2\text{Te}_4$ , the parameters are  $\gamma = 3.403 \text{ eV}\cdot\text{\AA}$ ,  $E_0 = 0 \text{ eV}$ ,  $D = 39.995 \text{ eV}\cdot\text{\AA}^2$ ,  $\Delta = 20 \text{ meV}$ ,  $B = 120 \text{ eV}\cdot\text{\AA}^2$ ,  $m_2 = 15.003 \text{ meV}$ ,  $\beta_1 = 8000 \text{ eV}\cdot\text{\AA}^3$ ,  $s_1 = 0 \text{ eV}\cdot\text{\AA}^2$ ,  $s_3 = 0 \text{ eV}\cdot\text{\AA}^2$ ,  $s_5 = 0 \text{ eV}\cdot\text{\AA}$ ,  $s_7 = 0 \text{ eV}\cdot\text{\AA}$ ,  $s_8 = 0 \text{ eV}\cdot\text{\AA}$  [54, 79].

**Appendix E: Relation between  $\mathcal{C}_i$  parameters in scaling law Eq. (3) and mechanisms in Fig. 1.** Below, the superscripts indicate mechanisms and 0 and 1 in the subscripts means static and dynamic scatterings, respectively. Four, three, and two digits in the subscripts mean the number of correlations of scattering events. See more details in Sec. SV of [74].

$$\begin{aligned} \mathcal{C}_4 &= (\mathcal{C}_{0000}^{2\text{SK}} - 4\mathcal{C}_{0001}^{2\text{SK}} + 6\mathcal{C}_{0011}^{2\text{SK}} - 4\mathcal{C}_{0111}^{2\text{SK}} + \mathcal{C}_{1111}^{2\text{SK}})\sigma_{xx0}^{-4} \\ &\quad + (\mathcal{C}_{000}^{2\text{SK}} - 2\mathcal{C}_{001}^{2\text{SK}} + \mathcal{C}_{011}^{2\text{SK}})\sigma_{xx0}^{-3} \\ &\quad + \mathcal{C}_{00}^{2\text{SK}}\sigma_{xx0}^{-2}, \\ \mathcal{C}_3 &= (4\mathcal{C}_{0001}^{2\text{SK}} - 12\mathcal{C}_{0011}^{2\text{SK}} + 12\mathcal{C}_{0111}^{2\text{SK}} - 4\mathcal{C}_{1111}^{2\text{SK}} \\ &\quad + \mathcal{C}_{000}^{\text{SSK}} - 2\mathcal{C}_{001}^{\text{SSK}} + \mathcal{C}_{011}^{\text{SSK}} - \mathcal{C}_{100}^{\text{SSK}} + 2\mathcal{C}_{101}^{\text{SSK}} - \mathcal{C}_{111}^{\text{SSK}})\sigma_{xx0}^{-3} \\ &\quad + (2\mathcal{C}_{001}^{2\text{SK}} - 2\mathcal{C}_{011}^{2\text{SK}} \\ &\quad + \mathcal{C}_{00}^{\text{SSK}*} - \mathcal{C}_{10}^{\text{SSK}*})\sigma_{xx0}^{-2}, \\ \mathcal{C}_2 &= (6\mathcal{C}_{0011}^{2\text{SK}} - 12\mathcal{C}_{0111}^{2\text{SK}} + 6\mathcal{C}_{1111}^{2\text{SK}} \\ &\quad + \mathcal{C}_{00}^{\text{SSK}} - 2\mathcal{C}_{01}^{\text{SSK}} + \mathcal{C}_{11}^{\text{SSK}} \\ &\quad + 2\mathcal{C}_{001}^{\text{SSK}} - 2\mathcal{C}_{011}^{\text{SSK}} + \mathcal{C}_{100}^{\text{SSK}} - 4\mathcal{C}_{101}^{\text{SSK}} + 3\mathcal{C}_{111}^{\text{SSK}} \\ &\quad + \mathcal{C}_{00}^{2\text{SJ}} - 2\mathcal{C}_{01}^{2\text{SJ}} + \mathcal{C}_{11}^{2\text{SJ}} \\ &\quad + \mathcal{C}_{00}^{\text{BSK}} - 2\mathcal{C}_{01}^{\text{BSK}} + \mathcal{C}_{11}^{\text{BSK}})\sigma_{xx0}^{-2} \\ &\quad + (\mathcal{C}_{011}^{2\text{SK}} + \mathcal{C}_{10}^{\text{SSK}*} + \mathcal{C}_0^{\text{SSK}} + \mathcal{C}_0^{\text{BSK}})\sigma_{xx0}^{-1} \\ &\quad + \mathcal{C}_{\text{Drude}}, \\ \mathcal{C}_1 &= (4\mathcal{C}_{0111}^{2\text{SK}} - 4\mathcal{C}_{1111}^{2\text{SK}} \\ &\quad + 2\mathcal{C}_{01}^{\text{SSK}} - 2\mathcal{C}_{11}^{\text{SSK}} + \mathcal{C}_{011}^{\text{SSK}} + 2\mathcal{C}_{101}^{\text{SSK}} - 3\mathcal{C}_{111}^{\text{SSK}} \\ &\quad + 2\mathcal{C}_{01}^{2\text{SJ}} - 2\mathcal{C}_{11}^{2\text{SJ}} \\ &\quad + 2\mathcal{C}_{01}^{\text{BSK}} - 2\mathcal{C}_{11}^{\text{BSK}} \\ &\quad + \mathcal{C}_0^{\text{BSJ}} - \mathcal{C}_1^{\text{BSJ}})\sigma_{xx0}^{-1}, \\ \mathcal{C}_0 &= \mathcal{C}_{1111}^{2\text{SK}} + \mathcal{C}_{11}^{\text{SSK}} + \mathcal{C}_{011}^{\text{SSK}} + \mathcal{C}_{101}^{2\text{SJ}} + \mathcal{C}_{11}^{\text{BSK}} + \mathcal{C}_1^{\text{BSJ}} + \mathcal{C}^{\text{QMD}}. \end{aligned} \quad (\text{E1})$$